ORIGINAL ARTICLE

Phase transition in electrorheological plasmas

Christopher Dietz | **Johannes Budak** | **Tobias Kamprich** |
Michael Kretschmer | **Markus H. Thoma**

I. Physikalisches Institut, Justus Liebig
Universität Giessen, Giessen, Germany

Correspondence
Markus H. Thoma, I. Physikalisches
Institut, Justus Liebig Universität Giessen,
Heinrich-Buff-Ring 16, D 35392 Giessen,
Germany.
Email: markus.h.thoma@physik.jlug.de

Abstract

Applying an external electric AC field to a dusty plasma, the micro-particles arrange in strings or chains. In analogy to electrorheological fluids, such a system is called electrorheological plasma. Turning gradually the AC field into a DC field, the string formation is diminished until it vanishes completely in the DC case. In this way, a cross-over transition from a string-like to an isotropic micro-particle many-body system can be investigated. Experimental investigations of electrorheological plasmas are performed under microgravity conditions in parabolic flights. For analysing the image data, a supervised machine learning code was developed and a continuous cross over was found. A molecular dynamics simulation showed qualitatively similar results but also some deviations from the experimental results.

KEYWORDS

dusty plasma, electrorheology, image analysis, MD simulations, microgravity research

1 | INTRODUCTION

Dusty or complex plasmas contain micron-sized particles ("dust grains") in addition to electrons, ions, and neutral atoms and molecules. Usually, they are generated by injecting micro-particles in low-temperature and low-pressure discharge plasmas. Due to the high mobility of the electrons in the low-temperature plasma, the micro-particles get negatively charged by collecting charged plasma particles. Depending on the size of the micro-particles, their charge is typically of the order 10^3 to 10^5 e causing a strongly coupled micro-particle system by the screened Coulomb interaction (Yukawa interaction) between them in the plasma. Structures and dynamics of large micro-particle systems containing up to 10^6 particles can easily be observed by laser illumination because of the large interparticle distance, typically more than $100\,\mu m$, resulting in a dilute and transparent particle system. Therefore, fundamental aspects of classical strongly coupled many-body physics can be studied on the level of individual particles in real time by image analysis.[1] Important examples are phase transitions in 2D and 3D systems, e.g. the transition of a complex plasma from liquid to crystalline state.[2] Even transitions between different crystalline states, bcc, and fcc, can be considered.[3]

Electrorheological fluids are non-conducting liquids containing nano- or microparticles which can change their properties drastically if external electric fields are applied.[4] For example, the viscosity can be enhanced by several orders of magnitude, caused by an induced attractive interaction of the particles in the direction of the applied electric field. Electrorheological fluids have important technological applications, e.g. for brakes and shock absorbers.[5] In the presence of an electric DC field in a complex plasma, an attractive interaction between the micro-particles is introduced by the ion streaming in the electric field. In this way, a wake potential behind the charged particles is produced which

can attract other downstream particles leading to the formation of particle strings, for example, in the plasma sheath where the charged micro-particles are levitated against gravity by the electric field of the sheath.[6] Such a system is non-Hamiltonian and Newton's third law is violated because the wake potential is asymmetric, i.e. the leading particle in the ion stream attracts the following one but not vice versa. Non-Hamiltonian many-body systems show interesting thermodynamic properties which can be studied in complex plasmas.[7] If an external AC field with a frequency much smaller than the ion plasma frequency but larger than the dust plasma frequency is applied to a complex plasma the, wake potential becomes symmetric due to the back and forth streaming ions around the stationary micro-particle resulting in a Hamiltonian interaction. For this purpose, the particles have to be located in the bulk plasma, which is possible under microgravity, where the electric field of plasma sheath does not disturb the string formation. Therefore, the first observation of an electrorheological plasma was done using the experiment PK-3 Plus on board the ISS.[8]

The experiment PK-4 ("Plasmakristallexperiment 4") was designed to investigate complex plasmas in a DC discharge which takes place in an elongated glass tube allowing, in particular, investigations of fluid phenomena. First microgravity experiments with PK-4 were performed in parabolic flights in 2003.[9] Since 2014, the flight model of PK-4 is operated on board the ISS. A detailed description of PK-4 can be found in ref. [10]. First investigations with PK-4 on electrorheological plasmas under microgravity have been conducted in parabolic flight campaigns in 2008 and 2009. For this purpose, the polarity of the longitudinal DC field was switched with a frequency of 1 kHz turning the DC field into an AC field. It was observed that string formation takes place only in the AC mode but was absent in the pure DC mode under identical conditions (particle size, gas pressure, DC current) which was attributed to the fact that non-Hamiltonian systems, i.e. applying a pure DC mode, are more unstable than Hamiltonian systems.[11]

In 2018, parabolic flight experiments with PK-4 were dedicated to the investigation of the phase transition from an isotropic system in the DC mode to a string system in the AC mode. For this purpose, a gradual duty cycle variation of the applied voltage was adopted from 50% (symmetric AC mode) to 0% (pure DC mode). Here, for example, a duty cycle of 40% corresponds to an asymmetric AC mode with 40% of the cycle at positive voltage and 60% at negative. In contrast to former experiments[8,11], where only the isotropic state or string formation was observed, we will now discuss for the first time the details of the phase transition, in particular, the dependence of the order parameter on the duty cycle, the order of the phase transition and the microscopic nature of the phase transition. These aims could only be realized in microgravity experiments, using a sophisticated image analysis and comparing the experimental results with MD simulations. Therefore, we will present in this paper these three steps in detail. In the next section, we will describe the experiments, before we will discuss our analysis method based on machine learning providing the results on the electrorheological phase transition. Afterward, we will introduce our molecular dynamics (MD) simulation for comparison. Finally, we will discuss our results and present our conclusions.

2 | EXPERIMENTS

The experiment facility PK-4 consists of the integrated base plate, on which the plasma chamber is mounted including several options for diagnostics and micro-particle manipulation (Figure 1), and the infrastructure composed of computers, vacuum pump and ventline, gas supply, container etc. The details are described in ref. [10]. Here, we will discuss only the components which are important for the following experiments. The plasma chamber is made of an elongated U-shaped glass tube with a diameter of 3 cm and a length of 86 cm in total. About 20 cm of the central part, where the positive column of the discharge is located, can be observed by two particle observation cameras with an adjacent field of view. At the ends of the glass tube, the high-voltage electrodes are mounted. The high-voltage power supply can be operated in a DC or AC mode (polarity switching) with a frequency up to 5 kHz. The DC current can be varied between 0.5 and 3 mA. The electric field strength of the longitudinal DC field in the positive column of the discharge was measured by Langmuir probes on ground in the absences of micro-particles to be about 2 V/cm almost independent of the DC current[10]. The gas, usually neon or argon with pressures between 10 and 200 Pa, is filled in by gas flow up to 10 sccm through the cylindrical electrode and can be pumped out through the other cylindrical electrode by a turbo molecular pump. After igniting the plasma, the micro-particles are injected from the dispensers through ports at the side legs of the glass tube. They are illuminated by a green laser diode (wave length 532 nm, power 20–140 mW), where the beam entering the main glass tube from one front side is converted by a lens into a thin laser sheet with a width of about 100 μm and a height of 18 mm. The scattered light from the micro-particles is recorded by two CCD cameras (2 Megapixel, 35 frames per second [fps] at full resolution) which can scan the tube 20 cm in horizontal direction as well as 3 cm perpendicular to it. The AC mode can be used to trap and stop the micro-particles since the net electric field vanishes for the massive particles if the frequency
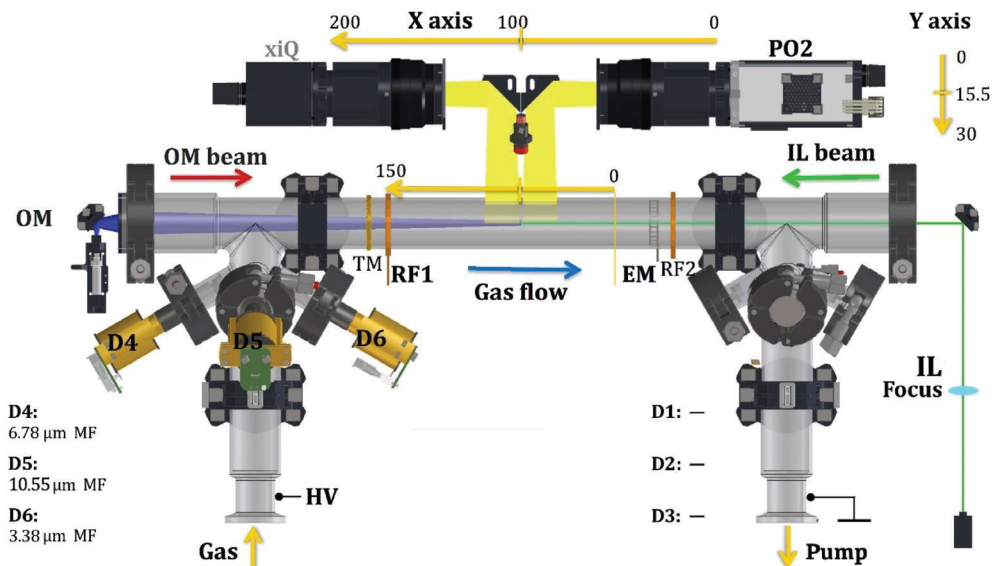
FIGURE 1 Schematic of the PK-4 plasma chamber adapted from ref. [10]
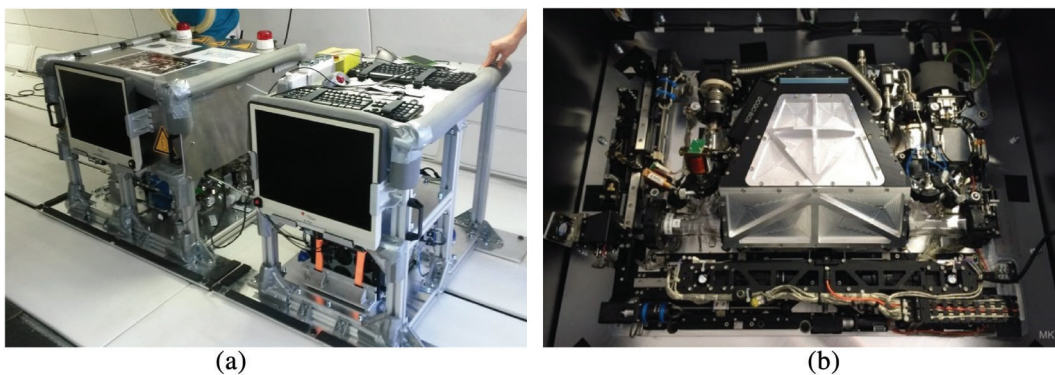
FIGURE 2 (a) The PK-4 parabolic flight experiment unit in the aircraft A310 Zero-G. (b) The integrated base plate accommodated in the left rack

of the AC filed is of the order of 100 Hz or higher. Further particle manipulation (external RF coils, manipulation laser, heating wire, internal electrode) and diagnostic (plasma glow observation camera, spectrometer) devices are attached to the plasma chamber but are not used for the following experiments.

The PK-4 parabolic flight experiment unit consists of two racks (Figure 2a), one containing the integrated base plate (Figure 2b), another one containing the computers for experiment control and recording. The integrated base plate was used as the engineering model for the ISS project and is to a large content identical with the one of the flight model. Compared to the flight model, we changed the following items: first we replaced one CCD camera by a CMOS camera with a larger field of view and a higher frame rate and resolution (xiQ MQ042MG-CM, 4 Megapixel, 90 fps at full resolution, 1 pixel corresponds to 11.4 μm). Second, we replaced the gas jet dispensers with the shaker dispensers which have a more reliable performance concerning the amount of injected micro-particles. The 31st DLR parabolic flight campaign took place in the aircraft A310 Zero-G of the company Novespace from February 26 to March 10, 2018 in Bordeaux. In the second week, there were four flight days with 31 parabolas per day. In each parabola, there was approximate weightlessness for about 22 s. The first and the third flight days were dedicated to electrorheology experiments. In the first day preparatory tests for determining appropriate experiment parameters, e.g. dispenser settings for optimizing the micro-particle amount, which could not be done on ground, were conducted. The plasma was ignited by a DC discharge in neon before the first parabola. The discharge current was 1 mA. The gas pressure was adjusted to 60 Pa for the first 10 parabolas and to 80 Pa for the following 10 parabolas leading to a subthermal ion flow in the positive column. In the last 11

parabolas, the pressure was 60 Pa and the discharge current was varied between 0.5 and 0.95 mA. Spherical micro-particles (melamine formaldehyde, diameter 6.86 μm, dispenser D4 in Figure 1) were injected at the beginning of the microgravity phase and transported by gas flow (0.4 or 0.6 sccm) to the field of view of the cameras. As soon as the particles appeared in the field of view, the gas flow was stopped and the polarity-switching mode was activated producing a longitudinal AC field with a frequency of 1 kHz in the plasma tube. The transport of the microparticles into the field of view of the cameras took about 2–3 s and the formation of strings about the same time. Therefore, there was about 10 s observation time of the electrorheological plasma in each parabola. The duty cycle was decreased from 50% to 0% in steps of 5% (apart from the last one which was 10%) from parabola 0 to 9 and again from parabola 10 to 19. In the last 11 parabolas, the duty cycle was fixed to 50%. If the duty cycle is different from 50%, the particles drift in the weak longitudinal net electric field. The particles were illuminated by a green laser sheet ("IL beam" in Figure 1) and recorded by both CCD and CMOS cameras. The quantitative analysis of the string formation depending on the duty cycle, the pressure, and the DC current is discussed in the next section. For this analysis, only the images of the CMOS camera were used.

3 | IMAGE ANALYSIS

The symmetry of stringlike particles in a complex plasma is relatively weak, in comparison, for example, with hexagonal crystal structures where six neighbouring particles have to be present in order to locally classify a single particle as crystalline. Therefore, it is challenging to have a precise local measurement of the stringlikeness in the neighbourhood of a particle. Previously applied methods for this problem are metrics based on anisotropic scaling index[8,11] and bond orientational order.[12] Another promising method are irreducible Minkowski tensors,[13] which are highly sensitive to anisotropy. The anisotropic scaling index is a good global measure, but failed at localized prediction (in our testing). The bond orientational order and irreducible Minkowski tensors on the other hand are local measures. However, we found that they are highly inaccurate due to the low symmetry of the particle chains. Additionally, the particle chains are often in dense or less dense regions of the dust cloud, which complicates the problem even more. Even with the naked eye, it is quite difficult to (locally) tell particle chains and isotropic particles apart.

To solve this challenging problem, we need a method that is local and reliable in a dataset of weak symmetry. Fortunately, the recent success of convolutional neural networks (CNN) showed that this method is well equipped to deal with a weak symmetry (as in the case of character recognition[14]). However, to be able to use this approach, we need to design a dataset to train the supervised machine learning model. The data itself has to consist of images that are either labelled as stringlike or isotropic. The usage of images means that it is possible to do the stringlike-classification directly on the experimental data without having to locate the particles first. Unfortunately, the experiments are done at different particle velocities due to the variation in duty cycle. Therefore, fast particles are recorded as elongated tracks instead of circular dots. To remove this complexity, we will calculate the particle positions first, using the open source software Trackpy.[15] The resulting point cloud can then be transformed to binary images of 24×24 pixels for every particle (Figure 3). We use a range of five average micro-particle distances d_{dust} in x and y direction of the image such that the beginning or end of a horizontal particle chain has to show at least three dust particles (using only two particles is possible, but too inaccurate for our needs). This provides localized information about the particle and its neighbours, such that a robust classification between stringlike and isotropic is possible.

The training data consist (in equal numbers) of examples of isotropic and anisotropic images. To label the images, we have to find enough examples of stringlike and isotropic particles in our experimental data. For the stringlike case, we manually select strongly stringlike regions in parts of our data and then analyse the point cloud of that region with a modified bond orientational order parameter p_n[12].

$$p_n(i) = \frac{2\pi}{(2n+1)N(i)} \sum_{j=1}^{N(i)} P_n(\cos(\theta_{ij})). \tag{1}$$

This parameter measures the stringlikeness of every particle in the point cloud. As the accuracy of this method is relatively low, we are only able to detect particles that are surrounded by stringlike neighbours. Therefore, beginning and end of a chain cannot be detected. Also, a lot of stringlike particles are missed by this method. For our analysis, the order $n = 2$ of the Legendre polynomial P_n was used. The number of neighbours is denoted as $N(i)$, while i is the index of the particle. (We used $N = 6$ nearest neighbours for the analysis). The angle θ_{ij} is the angle between two particles i and j. By using a threshold for p_n, we are able to choose particles with strong stringlike symmetry. These particles are then used
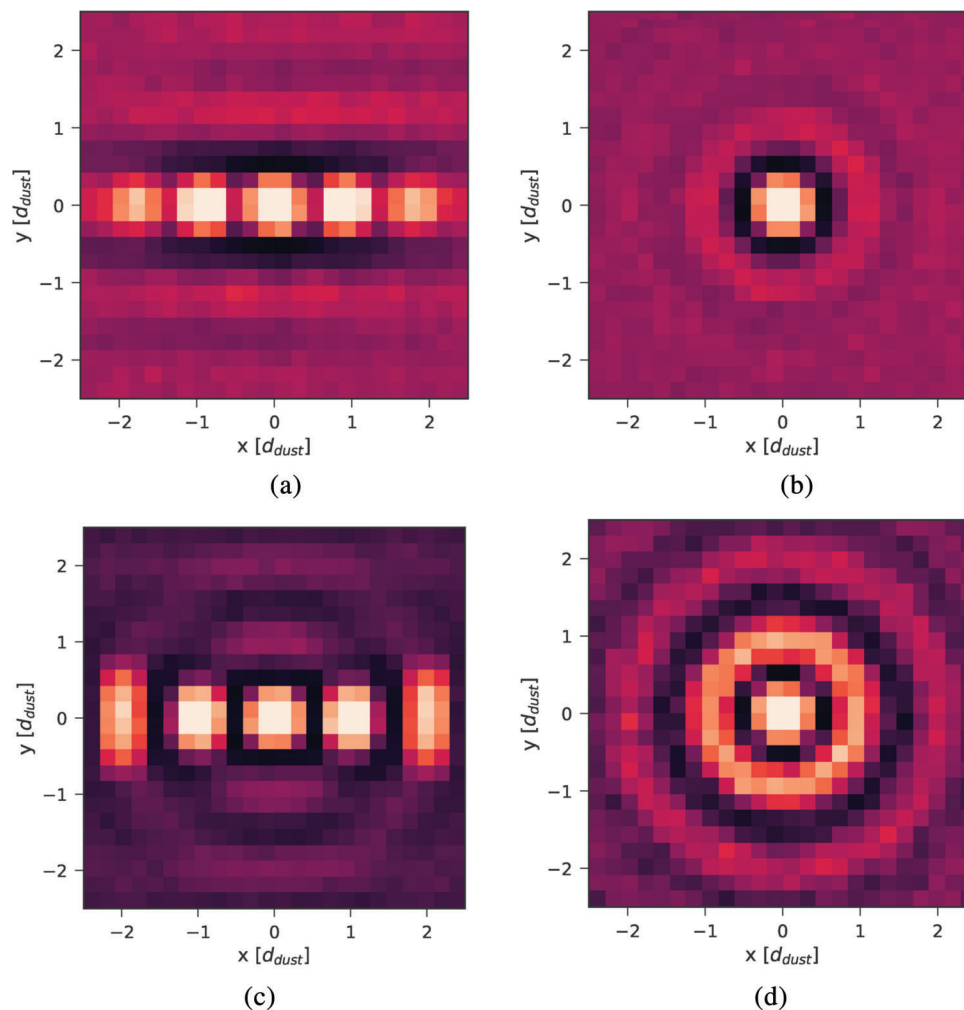
FIGURE 3   Statistical distribution of the training data in stringlike and isotropic cases for both artificial and experimental data. The images have 24×24 pixels covering a range of five micro-particle distances d_{dust}. (a) Experimental stringlike images. (b) Experimental isotropic images. (c) Artificially created stringlike images. (d) Artificially created isotropic images

to compose the training dataset of stringlike images (Figure 3a). As we are only able to retrieve some of the stringlike particles in our data, we cannot use this method to define isotropic particles.

Fortunately, in our parabolas with a current of 0.5 mA, no strings formed (see below). Therefore, we can easily use parts of these data as example for the isotropic case (Figure 3b). Now we have experimental data that are already labelled and can be used to train a machine learning model.

Unfortunately, the choice of labelling experimental data leads to another challenge. As we are only able to use parts of our experimental data where stringlike formations are most pronounced, our model will get a biased view of particle chains leading to significant classification errors. We mitigate this problem by randomly scaling the dust distances, such that dust density is no useful information for the machine learning model. The random scaling is needed because in previous attempts our machine learning model would not recognize particles in dense regions, because the bond orientational order parameter also does not work in dense regions. (The CNN needs to correctly generalize the problem and not reduce it to only density or number of particles). However, our tests showed that augmenting the experimental data is not enough to solve this problem. Therefore, we add artificially created data of stringlike and isotropic images (Figure 3c,d) to the training dataset.

The artificially created data ensure that our model generalizes the recognition of particle chains rather than learning patterns that are only specific to our experimental data. The artificial data are created by generating particles with similar statistical distribution to the experimental data. For the stringlike case (Figure 3c), a much higher deviation in the y axis is allowed compared to the experimental case (Figure 3a), which mitigates a limitation of our experimental data, because
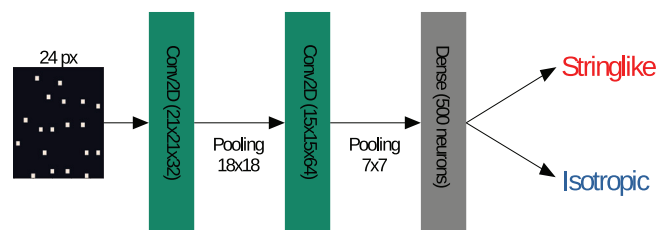
FIGURE 4   Schematic of the machine learning model. The model receives images of 24×24 pixels and outputs a stringlike or isotropic label

p_2 is only sensitive to horizontal chains. A random number generator is then used to place particles in a particle cloud according to the statistical distribution observed in the experiment. Then the point cloud is converted to images of 24×24 pixels. (This is identical to the experimental case).

Both experimental and artificial data combined in equal parts result in a dataset of 127196 images with 24×24 pixels. About 90% of the data is then used to train our machine learning model, while the remaining 10% is used for validation. The machine learning model itself will only briefly be discussed here (Figure 4). It consists of two convolutional layers (Conv2D), two maximum pooling layers (Pooling), and a final fully connected layer (Dense). The optimizer is a Nesterov Adam optimizer[16], which allows for fast convergence on the dataset. Regularization of the model is achieved with a 40% dropout layer.[17] The model has been implemented using the Keras API of the Tensorflow library.[18] The training takes 10 min on a Nvidia GTX 1080 Ti GPU and the accuracy on the validation dataset reaches 96.6 percent after 50 epochs.

After training, the machine learning model will classify every single particle in our experimental data as an image of 24×24 pixels spanning five micro-particle distances in x and y directions. This is done for a manually selected range of the frames in our parabolic flight videos. This manual selection is necessary because of disturbances in the dust cloud due to the residual acceleration in the airplane during the parabola. Therefore, the amount of detected strings can vary greatly during the parabola. (We have found this to be independent of the analysis method having a larger effect than noise). This motivated us to select a range of frames (but still consecutive) where the dust cloud was relatively undisturbed resulting in a more consistent percentage of stringlike particles in the cloud.

4 | RESULTS

Figure 5a shows a typical section of an image recorded in a parabolic flight experiment. Here the particle chains are clearly visible. In Figure 5b, the particles identified belonging to strings by the image analysis described above are indicated in red. In Figure 6, the percentage of particles found to be in strings compared to the total number of particles in the image is presented as a function of the duty cycle. At 60 Pa, first a slight increase of the string percentage up to a duty cycle of 35% is observed, followed by a steep decrease until duty cycle 0% where no strings are identified (Figure 6a). The unexpected increase at the beginning might be caused by residual accelerations of the aircraft ("G-jitter"). The steep decrease of the string formation below a duty cycle of 35% shows a clear phase transition from a stringlike to an isotropic system at a duty cycle around 20%. Using the string percentage as an order parameter, there is no indication for a first-order phase transition. At 80 Pa, no clear phase transition is seen although there is a decrease from duty cycle 20 to 0% (Figure 6b). The string percentage at duty cycle 50% is independent of the current between 0.6 and 1 mA. However, below 0.6 mA, a clear decrease of the string formation is observed (Figure 6c), probably caused by unstable discharge conditions at low currents.

5 | MOLECULAR DYNAMICS SIMULATION

In order to compare our experimental results with theoretical results, we performed numerical simulations based on molecular dynamics (MD). For this purpose, the open source program LAMMPS (https://lammps.sandia.gov/) was adopted.[19] First, the interaction potential between the particles has to be incorporated into the program. In addition to the repulsive Yukawa interaction, the wake interaction between the micro-particles in the presence of an ion drift has to
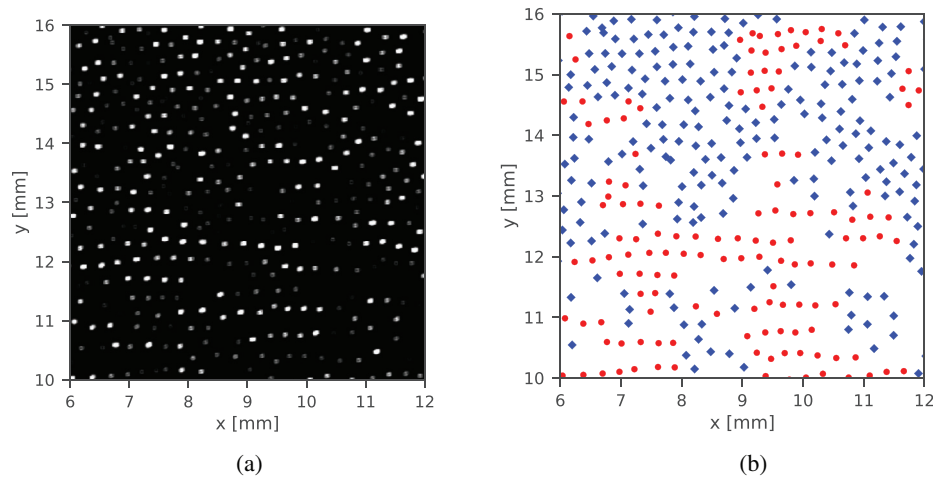
FIGURE 5 Strings in experimental data. (a) $6 \times 6\,\mathrm{mm}^2$ section of a typical image showing strings (image enhanced for better visibility). (b) Result of image analysis applied to left image. Particles found to be in strings marked red, others blue

be taken into account. In ref. [20], the following expression for such a potential in case of small (subthermal) ion flow velocities v_{fl}, as they are realized in the experiment, was proposed:

$$\varphi(\mathbf{r}) = \varphi_0(r) + v_{fl}\varphi_1(r)\cos\theta + v_{fl}^2\varphi_2(r)\cos^2\theta + v_{fl}^2\varphi_3(r)\sin^2\theta + o(v_{fl}^2). \qquad (2)$$

The functions $\varphi_{0,1,2,3}(r)$ are given by

$$\varphi_0(r) = \frac{e^{-r\sqrt{1+\tau}}}{r}, \qquad (3)$$

$$\varphi_1(r) = -\frac{2}{\pi r^2}\int_0^\infty \frac{kr\cos kr - \sin kr}{(k^2+1+\tau)^2} \cdot g_1(\nu/k)dk, \qquad (4)$$

$$\varphi_2(r) = -\frac{2}{\pi r^3}\int_0^\infty \frac{2kr\cos kr + (k^2r^2-2)\sin kr}{k(k^2+1+\tau)^3} \times [g_2(\nu/k)(k^2+1+\tau) + g_1^2(\nu/k)]dk, \qquad (5)$$

$$\varphi_3(r) = \frac{2}{\pi r^3}\int_0^\infty \frac{kr\cos kr - \sin kr}{k(k^2+1+\tau)^3} \times [g_2(\nu/k)(k^2+1+\tau) + g_1^2(\nu/k)]dk. \qquad (6)$$

Here ν is the collision frequency, $\tau = T_i/T_e$ the ion-to-electron temperature ratio, and $g_{1,2}(x)$ two auxiliary functions defined as

$$g_1(x) = \frac{\mathrm{erfcx}(x/\sqrt{2})}{-\sqrt{2/\pi} + x\,\mathrm{erfcx}(x/\sqrt{2})},$$

$$g_2(x) = \frac{\sqrt{2\pi}x(7-x^2)\mathrm{erfcx}(x/\sqrt{2}) - 4\pi x^2\mathrm{erfcx}(x/\sqrt{2}) + 2x^2 - 8}{[2 - \sqrt{2\pi}x\,\mathrm{erfcx}(x/\sqrt{2})]^2}$$

with the scaled complementary error function erfcx(x). The expression in Equation (2) and the functions in (3–6) are normalized as:

$$\frac{\varphi}{Q/4\pi\epsilon_0\lambda} \to \varphi, \frac{\nu}{\omega_p} \to \nu, \frac{\mathbf{v}_{fl}}{v_{T_i}} \to \mathbf{v}_{fl}, \frac{\mathbf{r}}{\lambda} \to \mathbf{r}, \qquad (7)$$

with the characteristic length λ defined as the ratio of thermal ion velocity v_{T_i} and plasma frequency ω_p of the ions, and the micro-particle charge Q.
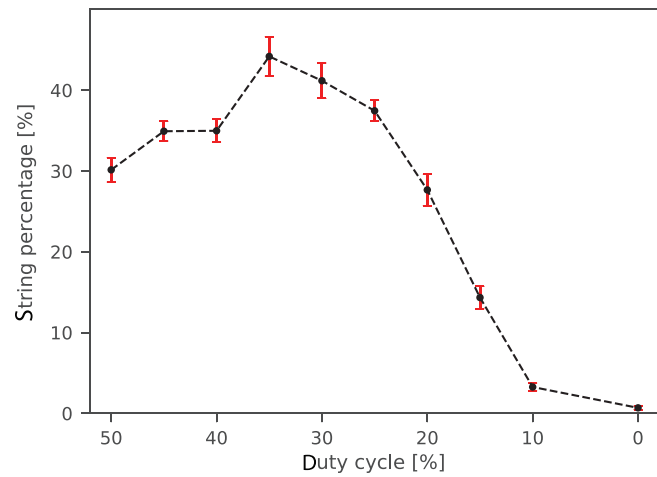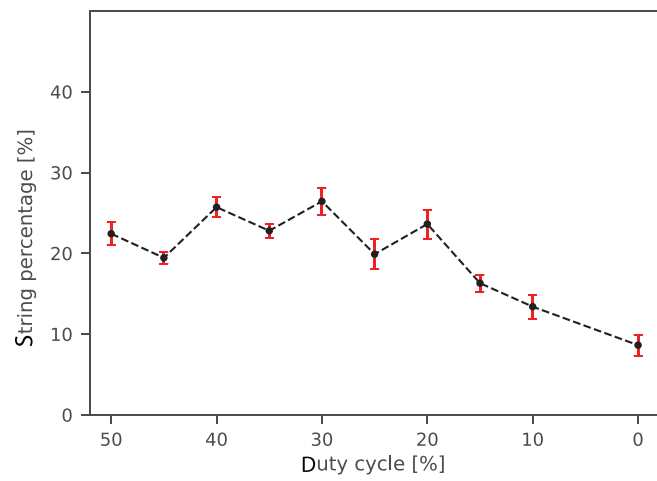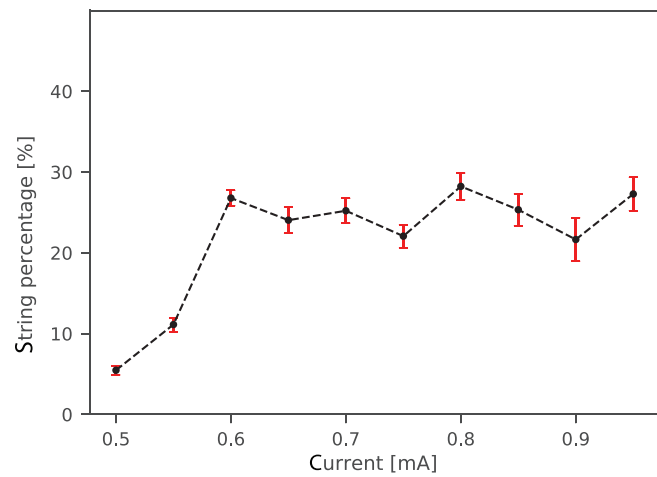
FIGURE 6 String percentage depending on duty cycle and current at pressures of 60 and 80 Pa. (a) 60 Pa. (b) 80 Pa. (c) 60 Pa

For determining these parameters, the electron density and temperature in PK-4 measured by Langmuir probes were assumed. These measurements showed approximately linear dependence of these quantities on the pressure[21]:

$$n_e = (0.9 + 0.03 p[Pa]) \times 10^{14} m^{-3},$$
$$T_e = (8.3 - 0.02 p[Pa]) eV. \tag{8}$$

The characteristic length $\lambda = v_{T_i}/\omega_p$, can be estimated by calculating the plasma frequency[20].

$$\omega_\mathrm{p} = \sqrt{\frac{n_i \cdot e^2}{\varepsilon_0 \cdot m_i}}$$

and the thermal velocities of the ions $v_{T_i} = \sqrt{T_i/m_i} = 378$ ms^{-1} by assuming room temperature $T_i = 0.03\,eV$. The collision frequency v can be estimated by the Bhatnagar–Gross–Krook-Model to[22]:

$$v \approx \frac{1}{0.341} \cdot \frac{v_{T_i}}{\ell_i}, \tag{9}$$

with the ion mean-free path given by

$$\ell_i = \frac{1}{n_n \sigma}, \tag{10}$$

where n_n is the neutral gas particle density following from the ideal gas equation of state from the pressure and the collision cross section in neon $\sigma = 21 \times 10^{-20}$ m^2 [23]. The micro-particle charge Q was calculated following ref. [21] by equating the ion current and the electron current to the micro-particle surface, where the ion current is given by

$$I_i \approx \sqrt{8\pi} a^2 n_i v_{T_i} z\tau [1 + 0.1 z\tau(\lambda/\ell_i)] \tag{11}$$

and the electron current by

$$I_e = \sqrt{8\pi} a^2 n_e v_{T_e} \exp(-z). \tag{12}$$

Here a is the micro-particle radius, $z = Ze^2/aT_e$ the dimensionless micro-particle charge, and $v_{T_e} = \sqrt{T_e/m_e}$ with electron mass m_e. Assuming $0.1(z/\tau)(\lambda/l_i) \gg 1$ and $z \lesssim 1$, the expression for z can be simplified to[21].

$$z \approx 3\tau \sqrt{\frac{v_{T_e}}{v_T}} \cdot \sqrt{\frac{l_i}{\lambda}}, $$

from which the particle charge can be calculated. Furthermore, the Mach number v_{fl}, i.e. ratio of ion drift velocity to thermal ion velocity, has to be taken into account. For experiments with PK-4 using a Neon plasma, the pressure-dependent Mach number is given by $v_{fl} \simeq 22/p[Pa]$[11]. The pressures adopted in the experiment of 60 and 80 Pa correspond therefore to subthermal ion velocities in the positive column. In addition to these parameters, the neutral drag force of the micro-particles in the gas background is required for the MD simulation. Following the work by Epstein[24], the neutral drag of a spherical particle in a gas is given by

$$F = -m\gamma v, \tag{13}$$

where v is the relative velocity of the particle to the gas, m the micro-particle mass, and γ the damping coefficient.

$$\gamma = \delta \frac{n_n m_n v_{T_n}}{\rho a} \tag{14}$$

with density $\rho = 1.5$ g/cm^3 for melamine formaldehyde micro-particles, m_n the mass of the gas particles, and v_{T_n} their thermal velocity. The accommodation coefficient $\delta = 1.48$ was adopted according to ref. [25].

TABLE 1 Calculated Plasma- and simulation parameters

Pressure (p in Pa)	60	80			100
Normalized drift velocity (v_{fl})	11/15	0.55			0.44
Characteristic length (λ in μm)	39.18	35.44			32.6
Normalized collision frequency (ν)	0.3	0.36			0.42
Neutral to electron temperature ratio (τ in 10^{-3})	4.23	4.48			4.76
Micro-particle radius (a in μm)	3.14	2.4	3.14	6.8	3.14
Micro-particle charge (Q in 10^4 e)	3.32	2.28	2.99	6.47	2.74
Damping coefficient (γ^{-1} in μs)	20,088	11,516	15,066	32,627	12,053
Micro-particle mass (m in pg)	194.52	86.86	194.52	1,975.63	194.52

However, with these calculations the resulting wake potential was not suitable for simulating string formation since the attractive part of the potential is not within the limits of the intermediate particle distances. Therefore, the following parameter adjustments have been made:

$$\omega_p' = 2 \cdot \omega_p \tag{15}$$

$$v_{fl}' = 2 \cdot v_{fl} = 44/p. \tag{16}$$

These adjustments are justified considering the homogeneous plasma approximation made deriving the potential[20] and other uncertainties e.g. in the measurement of the longitudinal electric field by a Langmuir probe. Doubling the plasma frequency cuts the characteristic length λ and the normalized collision frequency ν in half, which shifts the minimum of the wake potential towards the region of the particles distances and thus making string formation possible. For taking into account the neutral drag force on the particles in the simulation, a Langevin thermostat was applied. The total force acting on a particle is then given by

$$F = F_c + F_f + F_r,$$
$$F_f = -m\gamma v,$$
$$F_r \propto \sqrt{\frac{k_B T m \gamma}{dt}},$$

where F_c is the interparticle force following from the interparticle potential given above and dt is the time step chosen as 0.1 μs in the simulation. The parameters used in the simulation are shown in Table 1 for three different neon pressures and different micro-particle sizes used in the MD simulation.

In a first step, the interaction energy $E(\mathbf{r}) = Q \cdot \varphi(\mathbf{r})$ was calculated. In order to take the duty cycle variation into account, the interaction energies in z-direction and $-z$-direction were superimposed. Therefore, the potential in Equation (2) is expressed in cylindrical coordinates with the ion flow set in the z-axis as follows:

$$\varphi(z, \rho) = Q \left[\varphi_0(z, \rho) + v_{fl} \varphi_1(z, \rho) \cdot \frac{z}{\sqrt{z^2 + \rho^2}} + v_{fl}^2 \varphi_2(z, \rho) \cdot \frac{z^2}{z^2 + \rho^2} \right.$$
$$\left. + v_{fl}^2 \varphi_3(z, \rho) \left(1 - \frac{z^2}{z^2 + \rho^2} \right) \right]. \tag{17}$$

For example, for a duty cycle of 40% the energy $0.4E(z, \rho) + 0.6E(-z, \rho)$ has been used. Figure 7 shows the plot of the energy along the ion flow for three different duty cycles. Whereas the attractive part for duty cycle 0% appears only in negative z-direction, the energy becomes symmetric in the z-direction at duty cycle 50%. The pressure dependence using a duty cycle of 50% is plotted in Figure 8 showing a weaker attraction for larger pressures. The attractive part of the interaction potential can be approximated by a dipole–dipole interaction[8] and is proportional to the square of the Mach number. Since the Mach number is proportional to $1/p$, a reduction of the attraction with increasing pressure follows. Also the depth of the attractive potential is larger for larger particles than for smaller ones which is not shown here.
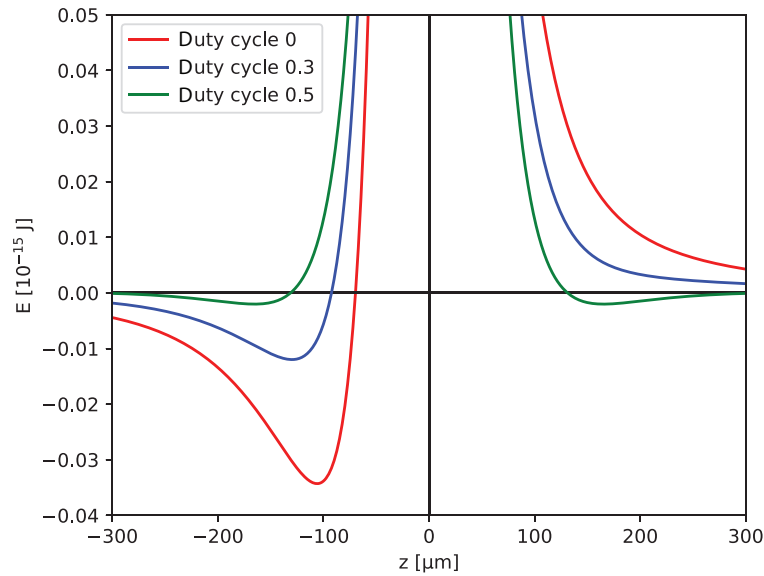
FIGURE 7   Interaction energy along the ion flow at 80 Pa and a particle radius of 3.14 μm for three different duty cycle
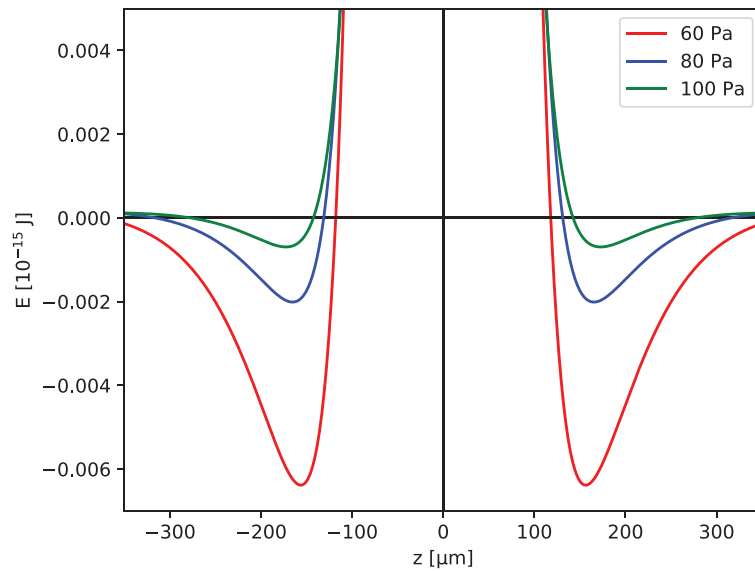
FIGURE 8   Interaction energy along the ion flow at a duty cycle of 0.5 and a particle radius of 3.14 μm for three different pressures

The simulations were performed in a lattice box under periodic boundary conditions containing 1,000 simple cubic (sc) unit cells with a lattice spacing of 200 μm each holding one particle. The dimensions of the box are 10,000 μm × 4,000 μm × 200 μm. Since the width of the z-dimension in the simulation area is set to be only one unit cell containing one particle, the simulations can be considered as two-dimensional. Therefore, the image analysis algorithm introduced above is also applicable to the simulation data. The longest side of the simulation box corresponds to the ion flow direction and thus where string formation is expected. Each simulation runs for 2,000,000 timesteps corresponding to 200 ms in total. Figure 9 shows the particle formation at the end of the simulation for three different duty cycles at a pressure of 80 Pa and a particle radius of 3.14 μm. Not only almost purely isotropic (Figure 9a) and stringlike (Figure 9c) systems are visible, but also stringlike and isotropic constellations occurring commonly in one system (Figure 9b). It was found that the string formation is impaired in the case of small duty cycles because the initially formed particle chains collide with particles which are not part of a chain due to the fact that the particles start to move in an asymmetric interaction potential.

(a)

(b)

(c)
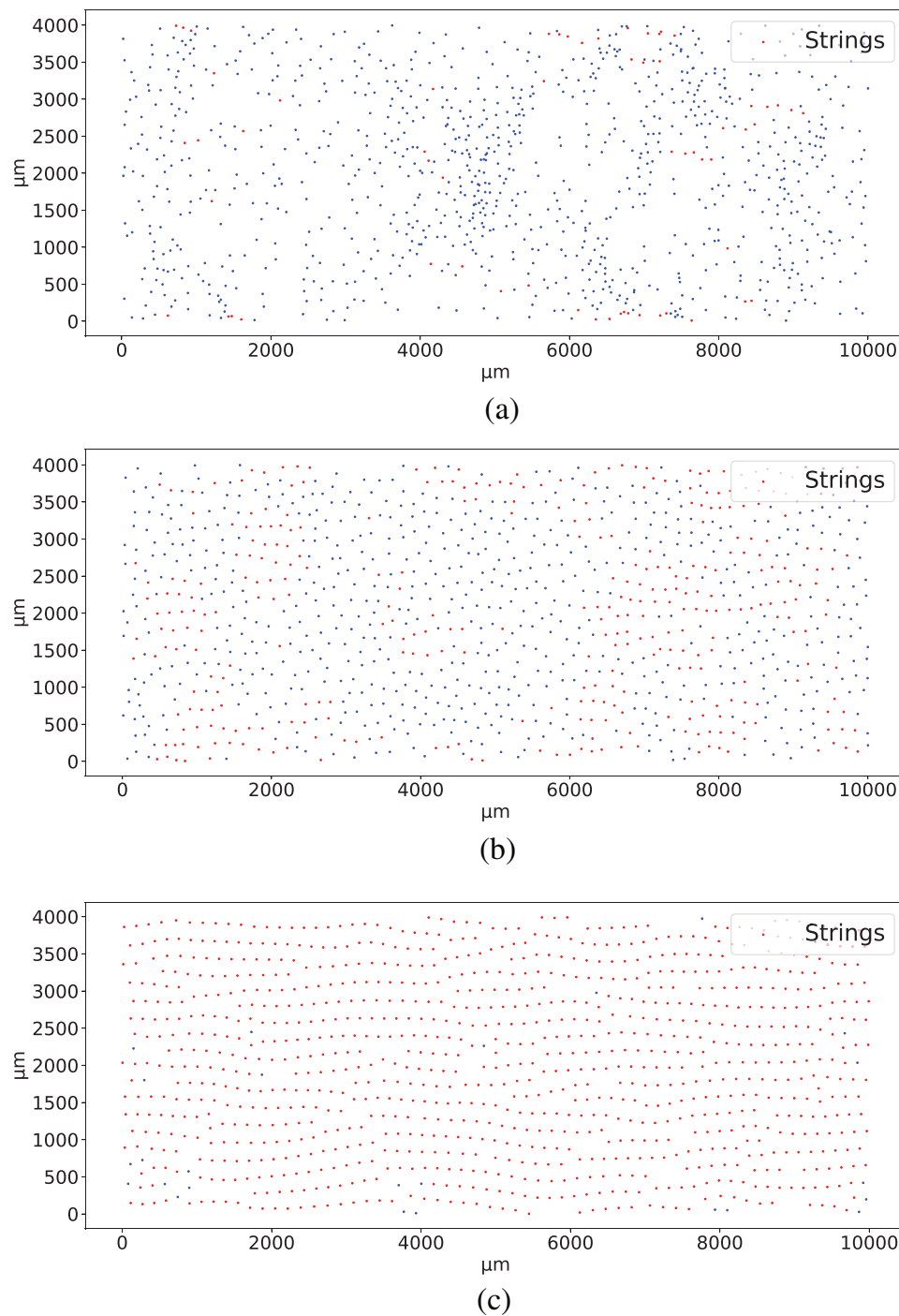
FIGURE 9 Particle formation after 2,000,000 timesteps for a particle radius of 3.14 μm and a pressure of 80 Pa for different duty cycle. Particles found to be in strings marked red, others blue. (a) Duty cycle 0%. (b) Duty cycle 35%. (c) Duty cycle 50%

In the experiment, the particles drift due to the presence of a longitudinal net electric field and also collide with other particles. This is the microscopic explanation for the absence of strings in the case of a DC field (non-Hamiltonian system), although an attractive wake potential is present, and the presence of strings in the AC field (Hamiltonian system) already observed in former experiments[11]. After about 1,500,000 timesteps, depending on the duty cycle, the string formation reaches an equilibrium. So the string percentage is subsequently calculated as the average of the last 500,000 timesteps, with the SD considered as error bar. The string formation as a function of the duty cycle for a particle radius of 3.14 μm at pressures of 60, 80, and 100 Pa is plotted in Figure 10.
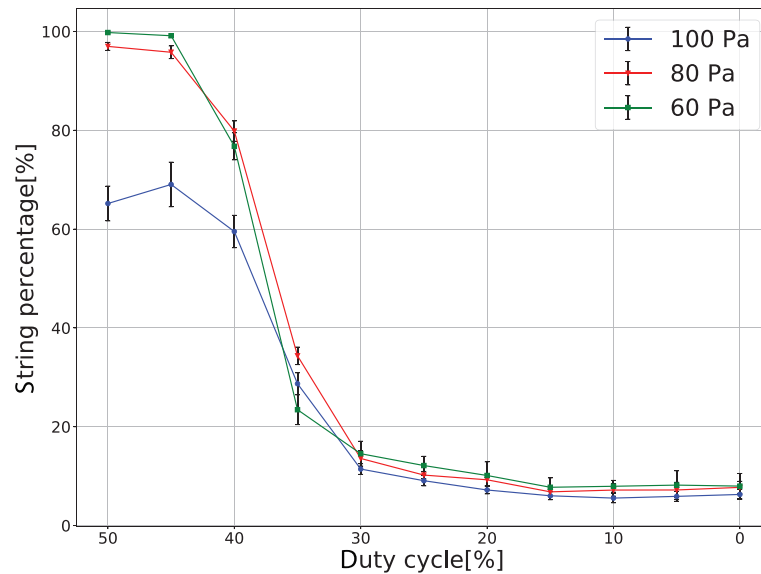
FIGURE 10   String formation at 60, 80, and 100 Pa for 5,000 particles with radius 3.14 μm. The error considered is the SD of the last 500,000 timesteps
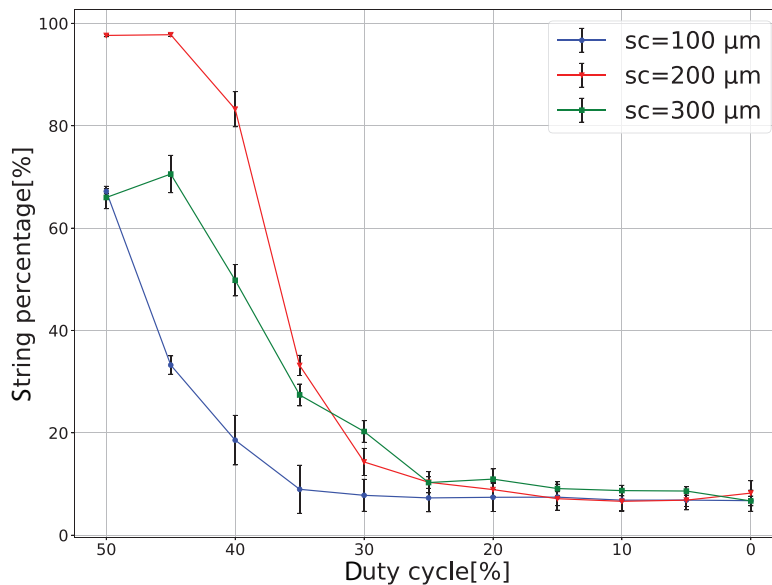
FIGURE 11   String percentage vs. duty cycle for different lattice spacings at a pressure of 80 Pa and a particle radius of 3.14 μm

Clearly a higher order continuous phase transition (cross over) is visible in qualitative agreement with the experiment. While the string percentages for 60 and 80 Pa are quite similar, a decreasing string alignment is distinctly observable at 100 Pa. That as well qualitatively corresponds to the experiment, where less strings are formed by increasing the pressure.

In Figure 11, the particle density is varied by using different lattice spacings (100, 200, and 300 μm). In order to optimally form strings, the intermediate particle distance has to be within the attractive part of the potential for 80 Pa (seen in Figure 8). Consequently, Figure 11 shows the highest string percentages at a lattice spacing of 200 μm and the lowest at 100 μm. Nevertheless, a cross-over phase transition is observable for all three spacings.

Overall, the curves obtained from the simulations show similar gradients as in the experiments. Due to the uncertainties of the wake potential, the plots for different pressures do not exactly match with the experiments; however, they show the same correlation of decreasing string formation with increasing pressure.

6 | CONCLUSIONS

The electrorheological phase transition from a stringlike to an isotropic micro-particle many-body system in a complex plasma in the presence of an external electric field has been investigated in microgravity experiments using the facility PK-4 and in MD simulations. These experiments are only possible under microgravity where the micro-particles are located in the centre of the tube and are not disturbed by the radial electric field of the plasma sheath. Here, experiments were performed in short-term and approximate microgravity conditions in parabolic flights. The longitudinal electric field has been gradually changed from a symmetric AC field to a DC field by varying the duty cycle of the applied voltage from 50% to 0%. Because of the weak one-dimensional symmetry of stringlike systems, a sophisticated image analysis is required for which we chose an analysis based on supervised machine learning.

As reported earlier, string formation (electrorheology) was found in the AC case corresponding to a Hamiltonian system with symmetric interaction potential between the micro-particles, whereas an isotropic system was observed in the pure DC case in which the wake potential is non-reciprocal corresponding to a non-Hamiltonian system. Decreasing the duty cycle from 50% to 0%, for the first time a transition was observed with a continuously decreasing order parameter (string percentage) corresponding to a cross over at a gas pressure of 60 Pa. A much less pronounced transition was observed at 80 Pa. No dependence on the electric current was detected apart from a decrease of the string formation for very low currents (below 0.6 mA), which might be caused by unstable plasma conditions at low currents.

MD simulations based on the code LAMMPS including a non-analytical wake potential between the micro-particles have been conducted. They showed qualitatively similar results as the experiments, namely, a gradual transition from a stringlike system to an isotropic if the duty cycle is varied and a decrease of string formation for higher pressures. The details of this transition depend sensitively on the pressure, particle size, and particle density. The simulation allowed a microscopic explanation of the absence of string formation in the pure DC case in spite of the presence of an attractive wake potential, namely, the particle drift in the case of an asymmetric potential leading to collisions between particles inside and outside of initially formed chains preventing string formation.

In conclusion, for the first time, the physics of the phase transition, namely, the order of the transition and its microscopic nature, in an electrorheological plasma have been investigated in microgravity experiments and MD simulations.

Differences between experiment and simulation may be caused by residual accelerations in the aircraft, variations in the particle density or deviations from the potential assumed in the simulation. In addition, due to various approximations made deriving the potential[20], some adjustments of the calculated parameters had to be made in order to approximate the experimental results. Electrorheological experiments with PK-4 on board the ISS, where undisturbed long-term microgravity conditions exist, might help to clarify these questions.

DATA AVAILABILITY STATEMENT

Data available on request from the authors.

REFERENCES

[1] A. Ivlev, H. Loewen, G. Morfill, C. P. Royall, Complex Plasmas and Colloidal Dispersions: Particle-Resolved Studies of Classical Liquids and Solids, Vol. *5*, World Scientific Publishing Company, Hackensack, NJ, **2012**.

[2] H. M. Thomas, G. E. Morfill, *Nature* **1996**, *379*, 806.

[3] C. Dietz, T. Kretz, M. Thoma, *Phys. Rev. E* **2017**, *96*, 011301.

[4] W. M. Winslow, *J. Appl. Phys.* **1949**, *20*, 1137.

[5] P. Sheng, W. Wen, *Ann. Rev. Fluid Mech.* **2012**, *44*, 143.

[6] O. Ishihara, S. V. Vladimirov, *Phys. Plasmas* **1997**, *4*, 69.

[7] A. Ivlev, J. Bartnick, M. Heinen, C.-R. Du, V. Nosenko, H. Löwen, *Phys. Rev. X* **2015**, *5*, 011035.

[8] A. Ivlev, G. Morfill, H. Thomas, C. Räth, G. Joyce, P. Huber, R. Kompaneets, V. Fortov, A. Lipaev, V. Molotkov, T. Reiter, M. Turin, P. Vinogradov, *Phys. Rev. Lett.* **2008**, *100*, 095003.

[9] M. Thoma, H. Höfner, M. Kretschmer, S. Ratynskaia, G. Morfill, A. Usachev, A. Zobnin, O. Petrov, V. Fortov, *Micrograv.-Sci. Technol.* **2006**, *18*, 47.

[10] M. Pustylnik, M. Fink, V. Nosenko, T. Antonova, T. Hagl, H. Thomas, A. Zobnin, A. Lipaev, A. Usachev, V. Molotkov, O. F. Petrov, V. E. Fortov, C. Rau, C. Deysenroth, S. Albrecht, M. Kretschmer, M. H. Thoma, G. E. Morfill, R. Seurig, A. Stettner, V. A. Alyamovskaya, A. Orr, E. Kufner, E. G. Lavrenko, G. I. Padalka, E. O. Serova, A. M. Samokutyayev, S. Christoforetti, *Rev. Sci. Instrum.* **2016**, *87*, 093505.

[11] A. V. Ivlev, M. H. Thoma, C. Räth, G. Joyce, G. E. Morfill, *Phys. Rev. Lett.* **2011**, *106*, 155001.

[12] P. Brandt, A. V. Ivlev, G. E. Morfill, *J. Magn. Magn. Mater.* **2011**, *323* Proceedings of 12th International Conference on Magnetic Fluid, 1368.

[13] G. E. Schroeder-Turk, W. Mickel, S. C. Kapfer, F. M. Schaller, B. Breidenbach, D. Hug, K. Mecke, *N. J. Phys.* **2013**, *15*, 083028.

[14] D. C. Cireşan, U. Meier, L. M. Gambardella, J. Schmidhuber, *Neural Comput.* **2010**, *22*, 3207.

[15] D. Allan, T. Caswell, N. Keim, C. van der Wel, trackpy: Trackpy v0.3.2 (**2016**).

[16] I. Sutskever, J. Martens, G. E. Dahl, G. E. Hinton, *ICML'13* **2013**, *28*, 5.

[17] N. Srivastava, G. Hinton, A. Krizhevsky, I. Sutskever, R. Salakhutdinov, *J. Machine Learn. Res.* **2014**, *15*, 1929.

[18] M. Abadi, A. Agarwal, P. Barham, E. Brevdo, Z. Chen, C. Citro, G. S. Corrado, A. Davis, J. Dean, M. Devin, S. Ghemawat, I. Goodfellow, A. Harp, G. Irving, M. Isard, Y. Jia, R. Jozefowicz, L. Kaiser, M. Kudlur, J. Levenberg, D. Mané, R. Monga, S. Moore, D. Murray, C. Olah, M. Schuster, J. Shlens, B. Steiner, I. Sutskever, K. Talwar, P. Tucker, V. Vanhoucke, V. Vasudevan, F. Viégas, O. Vinyals, P. Warden, M. Wattenberg, M. Wicke, Y. Yu, X. Zheng, TensorFlow: Large-scale machine learning on heterogeneous systems (**2015**), software available from tensorflow.org.

[19] S. Plimpton, *J. Computat. Phys.* **1995**, *117*, 1.

[20] R. Kompaneets, G. E. Morfill, A. V. Ivlev, *Phys. Rev. E* **2016**, *93*, 063201.

[21] S. Khrapak, S. V. Ratynskaia, A. Zobnin, A. Usachev, V. Yaroshenko, M. Thoma, M. Kretschmer, H. Höfner, G. Morfill, O. Petrov, V. E. Fortov, *Phys. Rev. E* **2005**, *72*, 016406.

[22] D. Else, R. Kompaneets, S. V. Vladimirov, *Phys. Plasmas* **2009**, *16*, 062106.

[23] R. N. Varney, *Phys. Rev.* **1952**, *88*, 362.

[24] P. S. Epstein, *Phys. Rev.* **1924**, *23*, 710.

[25] M. Schwabe, D. B. Graves, *Phys. Rev. E* **2013**, *88*, 023101.